

Marquette University

e-Publications@Marquette

Mathematics, Statistics and Computer Science Faculty Research and Publications Mathematics, Statistics and Computer Science, Department of (- 2019)

5-2017

EIT Imaging of Admittivities with a D-Bar Method and Spatial Prior: Experimental Results for Absolute and Difference Imaging

Sarah J. Hamilton

Marquette University, sarah.hamilton@marquette.edu

Follow this and additional works at: https://epublications.marquette.edu/mscs_fac



Part of the [Computer Sciences Commons](#), [Mathematics Commons](#), and the [Statistics and Probability Commons](#)

Recommended Citation

Hamilton, Sarah J., "EIT Imaging of Admittivities with a D-Bar Method and Spatial Prior: Experimental Results for Absolute and Difference Imaging" (2017). *Mathematics, Statistics and Computer Science Faculty Research and Publications*. 573.

https://epublications.marquette.edu/mscs_fac/573

EIT IMAGING OF ADMITTIVITIES WITH A D-BAR METHOD AND SPATIAL PRIOR: EXPERIMENTAL RESULTS FOR ABSOLUTE AND DIFFERENCE IMAGING

S. J. HAMILTON

ABSTRACT. Electrical Impedance Tomography (EIT) is an emerging imaging modality that uses harmless electrical measurements taken on electrodes at a body's surface to recover information about the internal electrical conductivity and or permittivity. The image reconstruction task of EIT is a highly nonlinear inverse problem that is sensitive to noise and modeling errors making the image reconstruction task challenging. D-bar methods solve the nonlinear problem directly, bypassing the need for detailed and time-intensive forward models, to provide absolute (static) as well as time-difference EIT images. Coupling the D-bar methodology with the inclusion of high confidence a priori data results in a noise-robust regularized image reconstruction method. In this work, the A Priori D-bar Method for complex admittivities is demonstrated effective on experimental tank data for absolute imaging for the first time. Additionally, the method is adjusted for, and tested on, time-difference imaging scenarios. The ability of the method to be used for conductivity, permittivity, absolute as well as time-difference imaging provides the user with great flexibility without a high computational cost.

1. INTRODUCTION

Electrical Impedance Tomography (EIT) is a portable, non-invasive imaging modality that applies low-amplitude low-frequency current through electrodes at the boundary of a body and measures the resulting voltages. These surface measurements then serve as boundary data in a mathematical inverse problem that is solved to determine the electrical conductivity and/or permittivity inside the body. There are a wide range of applications of EIT from monitoring heart and lung function of hospitalized patients to non-destructive evaluation of materials such as concrete. See [(Mueller and Siltanen, 2012, Chapter 12)] for further uses.

The electric potential $u(x, y)$ inside a simply-connected Lipschitz domain $\Omega \subset \mathbb{R}^2$ is modeled by the *admittivity equation*

$$(1) \quad \nabla \cdot (\gamma(x, y) \nabla u(x, y)) = 0,$$

where $\gamma(x, y) = \sigma(x, y) + i\omega\epsilon(x, y)$. The admittivity $\gamma(x, y)$ is comprised of the electrical conductivity $\sigma(x, y)$, electrical permittivity $\epsilon(x, y)$ and the angular frequency of the applied current ω . It is assumed that there exist positive constants σ_0 and E such that $\sigma(x, y) > \sigma_0$, $\|\sigma\|_{W^{2,\infty}(\Omega)} \leq E$, and $\|\epsilon\|_{W^{2,\infty}(\Omega)} \leq E$.

The surface current and voltage measurements correspond to boundary conditions in the form of a *Neumann-to-Dirichlet* (ND), or ‘current density-to-voltage’, map $R_\gamma : \gamma \frac{\partial u}{\partial \nu}|_{\partial\Omega} \longrightarrow u|_{\partial\Omega}$, where ν denotes the outward-facing unit normal vector to the domain boundary $\partial\Omega$, whereas the *Dirichlet-to-Neumann* (DN) map is $\Lambda_\gamma : u|_{\partial\Omega} \longrightarrow \gamma \frac{\partial u}{\partial \nu}|_{\partial\Omega}$. Ensuring conservation of charge and specifying a ground, the DN map Λ_γ can be recovered as the inverse of the ND map. The inverse problem of EIT is then to recover the internal admittivity of an object through knowledge of the DN map (i.e. boundary measurements).

Reconstruction methods for EIT can be broken down into two main categories: *iterative methods*, and *direct methods*. Most iterative methods solve an optimization problem to minimize the difference between the measured voltages (or a DN map) and the data predicted by a forward model that uses a guess conductivity/admittivity as its input for each iterate. This requires a fine-tuned forward model (accurate domain shape, precise locations of the electrodes, knowledge of the contact impedance at the electrode-skin interface, etc.) since (1) must be solved repeatedly to produce data for each iteration. See [Edic et al. (1998); Jain et al. (1997)] for examples of iterative methods for complex admittivity imaging.

Non-iterative/Direct Methods are mainly comprised of non-iterative linearized methods (e.g. Calderón (1980); Cheney et al. (1990)) and methods that solve the full nonlinear problem without iterations. The most common direct nonlinear methods are Bayesian inversion [Calvetti et al. (2015a,b); Kaipio et al. (2000)],

S. J. Hamilton is with the Department of Mathematics, Statistics, and Computer Science; Marquette University, Milwaukee, WI 53233 USA, email: sarah.hamilton@marquette.edu.

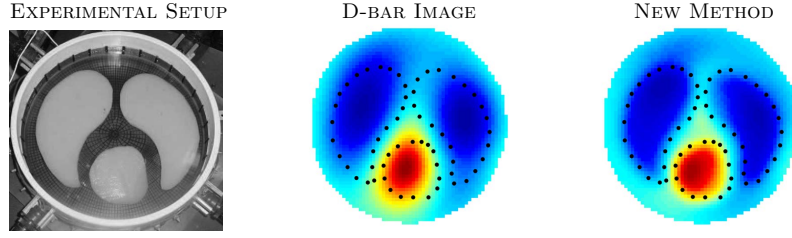


FIGURE 1. Demonstration of the *A Priori Absolute Imaging D-bar Method* on experimental data with an agar heart and lungs. Left: Experimental setup, Middle: D-bar reconstruction, Right: New method using *a priori* information displaying improved visualization of the lungs and heart. The reconstructed absolute conductivity is shown.

Factorization methods [Brühl (2001); Brühl and Hanke (2000); Brühl et al. (2003); Gebauer and Hyvönen (2007); Harrach and Seo (2009); Hyvönen (2007)], and D-bar methods [Astala and Päiväranta (2006a,b); Brown and Uhlmann (1997); Francini (2000); Knudsen et al. (2009); Mueller and Siltanen (2012); Nachman (1996); Novikov (1988)] which are capable of real-time thoracic imaging [Dodd and Mueller (2014)].

In many applications of EIT, at least some prior knowledge of the internal structure of the imaged body is known. Reconstruction methods that make use this *a priori* information have produced sharper EIT images [Avis and Barber (1995); Baysal and Eyüboğlu (1998); Dehghani et al. (1999); Dobson and Santosa (1994); Ferrario et al. (2012); Kaipio et al. (1999); Soleimani (2006); Vauhkonen et al. (1998)] and have been incorporated directly into the D-bar framework [Alsaker (2016); Alsaker and Mueller (2016); Hamilton et al. (2017)] by embedding the *a priori* knowledge into the direct nonlinear solution method.

Here we present the first absolute admittivity images recovered from experimental data using the admittivity D-bar method [Hamilton et al. (2012)]. Additionally, we develop an *a priori* D-bar framework for the time-difference imaging setting. We demonstrate the utility of the *a priori* admittivity D-bar methods for absolute and time-difference imaging, and present the first admittivity reconstructions using the methods on experimental data (see Figure 1). As the methods here are developed for the admittivity setting, they can be used for conductivity only, as well as admittivity EIT imaging.

The remainder of the manuscript is organized as follows. Section 2 provides a brief review of the D-bar for 2D Admittivity EIT imaging, and develops the *a priori* D-bar methods for absolute and time-difference imaging. In Section 3, the effectiveness of the methods is demonstrated for experimental EIT data: absolute as well as time-difference reconstructions are presented. A discussion of the results takes place in Section 4 and conclusions are drawn in Section 5. The reader is encouraged to view the manuscript on a computer screen for best visualization of the images as details may be masked in printed versions.

2. METHODS

This section provides a brief review of the 2D Admittivity D-bar framework and equations for admittivity image reconstructions based on [Francini (2000); Hamilton et al. (2012)]. Details of the numerical implementation can be found in [Hamilton and Mueller (2013); Hamilton et al. (2012); Herrera et al. (2015)].

2.1. Absolute Imaging with the D-bar Method. The D-bar method for complex admittivities is based on transforming the admittivity equation (1) to a first-order 2×2 system of special solutions, called *Complex Geometrical Optics solutions* (CGOs), that have a specific asymptotic behavior. These CGO solutions satisfy a ‘D-bar’ equation in a non-physical auxiliary variable (giving the method its name), from which the admittivity can then be recovered.

Two separate solutions $u_1(z, k)$ and $u_2(z, k)$ to the admittivity equation (1)

$$\nabla \cdot (\gamma(z) \nabla u_1(z, k)) = 0, \quad \text{and} \quad \nabla \cdot (\gamma(z) \nabla u_2(z, k)) = 0,$$

that are asymptotic to $\frac{e^{ikz}}{ik}$ and $\frac{e^{-ik\bar{z}}}{-ik}$, respectively, for large $|z|$ or $|k|$ are required for this method. Here and throughout we associate the physical space \mathbb{R}^2 with \mathbb{C} via $z = (x, y) \mapsto x + iy$, and $k \in \mathbb{C}$ denotes the

non-physical auxiliary parameter in the scattering domain. The ∂_z and $\bar{\partial}_z$ derivative operators are defined traditionally as $\partial_z = \frac{1}{2} \left(\frac{\partial}{\partial x} - i \frac{\partial}{\partial y} \right)$ and $\bar{\partial}_z = \frac{1}{2} \left(\frac{\partial}{\partial x} + i \frac{\partial}{\partial y} \right)$.

The admittivity equation (1) is transformed to the first-order system

$$(2) \quad [-D_k + Q(z)] M(z, k) = 0$$

using the change of variables

$$(3) \quad \begin{aligned} \begin{bmatrix} \Psi_{11}(z, k) & \Psi_{12}(z, k) \\ \Psi_{21}(z, k) & \Psi_{22}(z, k) \end{bmatrix} &= \gamma^{1/2}(z) \begin{bmatrix} \partial_z u_1(z, k) & \partial_z u_2(z, k) \\ \bar{\partial}_z u_1(z, k) & \bar{\partial}_z u_2(z, k) \end{bmatrix} \\ M(z, k) &= \Psi(z, k) \begin{bmatrix} e^{-ikz} & 0 \\ 0 & e^{ik\bar{z}} \end{bmatrix} \\ Q(z) &= \begin{bmatrix} 0 & -\frac{1}{2} \partial_z \log \gamma(z) \\ -\frac{1}{2} \bar{\partial}_z \log \gamma(z) & 0 \end{bmatrix}, \end{aligned}$$

where $D_k M(z, k) = \begin{bmatrix} \bar{\partial}_z & 0 \\ 0 & \partial_z \end{bmatrix} M(z, k) - ik \begin{bmatrix} 1 & 0 \\ 0 & -1 \end{bmatrix} \begin{bmatrix} 0 & M_{12}(z, k) \\ M_{21}(z, k) & 0 \end{bmatrix}$. It is assumed that $\gamma = 1$ in a neighborhood of $\partial\Omega$. The admittivity γ is extended from Ω into the plane by setting $\gamma(z) = 1$ for $z \in \mathbb{C} \setminus \Omega$. Readers familiar with the conductivity D-bar method [Nachman (1996)] will recognize (2) as an analog to the Schrödinger equation where here $Q(z)$ is a 2×2 matrix potential. Francini (2000) showed that (2) has a unique solution $M(\cdot, k)$ for $M(\cdot, k) - I \in L^p(\mathbb{R}^2)$ for some $p > 2$. The CGO solutions $M(\cdot, k)$ satisfy a D-bar equation in the k -variable

$$(4) \quad \bar{\partial}_k M(z, k) = M(z, \bar{k}) \begin{bmatrix} e(z, \bar{k}) & 0 \\ 0 & e(z, -k) \end{bmatrix} S(k).$$

where $S(k) = \begin{bmatrix} 0 & S_{12}(k) \\ S_{21}(k) & 0 \end{bmatrix}$ is the matrix of non-physical scattering data, a type of nonlinear Fourier transform data of the matrix potential. The admittivity is then recovered from the solution to the $\bar{\partial}_k$ equation (4) using the low-frequency CGO solutions $M(\cdot, 0)$ via

$$(5) \quad \gamma(z) = \exp \left\{ -\frac{2}{\pi \bar{z}} * Q_{12}(z) \right\} = \exp \left\{ -\frac{2}{\pi z} * Q_{21}(z) \right\},$$

where

$$(6) \quad Q_{12}(z) = \frac{\partial_z [M_{11}(z, 0) + M_{12}(z, 0)]}{M_{22}(z, 0) + M_{21}(z, 0)}, \quad \text{and} \quad Q_{21}(z) = \frac{\bar{\partial}_z [M_{22}(z, 0) + M_{21}(z, 0)]}{M_{11}(z, 0) + M_{12}(z, 0)}.$$

Letting $e(z, k)$ denote the unitary multiplier $e(z, k) = e^{i(kz + \bar{k}\bar{z})} = e^{2i\Re(zk)}$, the scattering data $S(k)$ is defined by

$$(7) \quad \begin{aligned} S_{12}(k) &= \frac{i}{\pi} \int_{\mathbb{C}} Q_{12}(z) e(z, -\bar{k}) M_{22}(z, k) d\mu(z) \\ S_{21}(k) &= -\frac{i}{\pi} \int_{\mathbb{C}} Q_{21}(z) e(z, k) M_{11}(z, k) d\mu(z), \end{aligned}$$

which can be written as the boundary integral equations, where ν denotes the outward unit normal vector to the boundary,

$$(8) \quad \begin{aligned} S_{12}(k) &= \frac{i}{2\pi} \int_{\partial\Omega} e^{-i\bar{k}z} \Psi_{12}(z, k) \nu(z) ds(z) \\ S_{21}(k) &= -\frac{i}{2\pi} \int_{\partial\Omega} e^{i\bar{k}\bar{z}} \Psi_{21}(z, k) \overline{\nu(z)} ds(z), \end{aligned}$$

that are evaluated using the current and voltage measurement data in the form of the DN map by solving

$$(9) \quad \begin{aligned} \Psi_{12}(z, k) &= \int_{\partial\Omega} \frac{e^{i\bar{k}(z-\zeta)}}{4\pi(z-\zeta)} (\Lambda_\gamma - \Lambda_1) u_2(\zeta, k) ds(\zeta) \\ \Psi_{21}(z, k) &= \int_{\partial\Omega} \overline{\left[\frac{e^{ik(z-\zeta)}}{4\pi(z-\zeta)} \right]} (\Lambda_\gamma - \Lambda_1) u_1(\zeta, k) ds(\zeta), \end{aligned}$$

where

$$(10) \quad \begin{aligned} u_1(z, k) &= \frac{e^{ikz}}{ik} - \int_{\partial\Omega} G_k(z - \zeta) (\Lambda_\gamma - \Lambda_1) u_1(\zeta, k) ds(\zeta) \\ u_2(z, k) &= \frac{e^{-ik\bar{z}}}{-ik} - \int_{\partial\Omega} G_k(-\bar{z} + \bar{\zeta}) (\Lambda_\gamma - \Lambda_1) u_2(\zeta, k) ds(\zeta), \end{aligned}$$

and Λ_1 is the DN map corresponding to a constant conductivity of one. The function $G_k(z)$ denotes the Faddeev Green's function [Faddeev (1966)], a special Green's function for the Laplacian, defined by

$$G_k(z) := e^{ikz} g_k(z), \quad -\Delta G_k = \delta$$

where

$$g_k(z) := \frac{1}{(2\pi)^2} \int_{\mathbb{R}^2} \frac{e^{iz \cdot \xi}}{\xi(\bar{\xi} + 2k)} d\xi,$$

for $k \in \mathbb{C} \setminus \{0\}$, where $z \cdot \xi = x\xi_1 + y\xi_2$, and $\xi = \xi_1 + i\xi_2$.

In the presence of noisy data, the fully nonlinear scattering data $S(k)$ is approximated by replacing the CGO solutions u_1 and u_2 by their asymptotic behaviors $\frac{e^{ikz}}{ik}$ and $\frac{e^{-ik\bar{z}}}{-ik}$ in the boundary integral equations (9) for Ψ_{12} and Ψ_{21} :

$$(11) \quad \begin{aligned} \Psi_{12}^{\text{exp}}(z, k) &= \int_{\partial\Omega} \frac{e^{i\bar{k}(z-\zeta)}}{4\pi(z-\zeta)} (\Lambda_\gamma - \Lambda_1) \frac{e^{-ik\zeta}}{-ik} ds(\zeta) \\ \Psi_{21}^{\text{exp}}(z, k) &= \int_{\partial\Omega} \left[\frac{e^{ik(z-\zeta)}}{4\pi(z-\zeta)} \right] (\Lambda_\gamma - \Lambda_1) \frac{e^{ik\zeta}}{ik} ds(\zeta), \end{aligned}$$

allowing for the introduction of ‘Born-type’ scattering data $S_{12}^{\text{exp}}(k)$ and $S_{21}^{\text{exp}}(k)$

$$(12) \quad \begin{aligned} S_{12}^{\text{exp}}(k) &= \frac{i}{2\pi} \int_{\partial\Omega} e^{-ikz} \Psi_{12}^{\text{exp}}(z, k) \nu(z) ds(z) \\ S_{21}^{\text{exp}}(k) &= -\frac{i}{2\pi} \int_{\partial\Omega} e^{i\bar{k}\bar{z}} \Psi_{21}^{\text{exp}}(z, k) \overline{\nu(z)} ds(z). \end{aligned}$$

Note that the superscript ‘exp’ signifies that the asymptotic behavior of the CGOs u_1 and u_2 has been used and $\overline{(\cdot)}$ denotes the complex conjugate of (\cdot) . The admittivity is then recovered using the approximate scattering data S^{exp} as summarized in the flowchart in Figure 2. An alternative S^{exp} formulation was introduced in [Herrera (2012); Herrera et al. (2015)] which requires the action of a tangential derivative map.

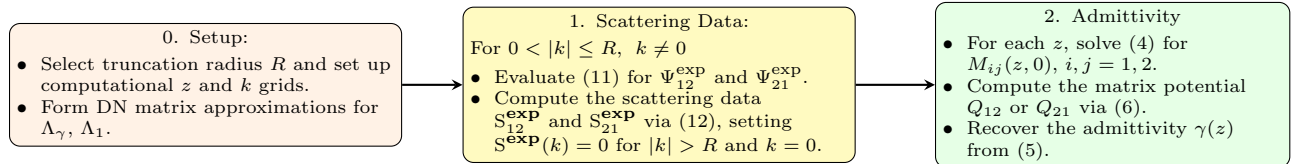


FIGURE 2. D-bar Method for Absolute Imaging

The D-bar method assumes $\gamma \approx 1$ near $\partial\Omega$. If this is not the case, following [Isaacson et al. (2004)], the best constant admittivity γ_{best} approximation to the data can be determined from the current and voltage data, and the DN map Λ_γ scaled to $\Lambda_{\tilde{\gamma}} = \frac{1}{\gamma_{\text{best}}} \Lambda_\gamma$. Then, $\Lambda_{\tilde{\gamma}}$ corresponds to the scaled admittivity $\tilde{\gamma} = \frac{\gamma}{\gamma_{\text{best}}}$ that is approximately one near the boundary. The DN map $\Lambda_{\tilde{\gamma}}$ is used in place of Λ_γ in Step 1 above, and the resulting admittivity $\tilde{\gamma}$ is then re-scaled by γ_{best} to recover γ in Step 3.

Notice that Steps 1 and 2 are trivially parallelizable in k and z , respectively, allowing for fast-computations. The low-pass filtering of the scattering data in Step 1 (setting $S(k) = 0$ for $|k| > R$) has a regularizing effect on the method, proven in [Knudsen et al. (2009)] to be a regularization strategy for the 2D conductivity case. Low-pass filtering of Fourier data is known to lead to a loss of sharp edges which we also see for the non-physical scattering data. In fact, note that for large $|k|$ frequencies, using the asymptotic conditions of the CGO solutions $M(z, k)$ in (7), the scattering data is essentially shifted Fourier data for the potential Q ,

$$S_{12} \equiv \frac{i}{\pi} \widehat{Q_{12}}(2k_1, 2k_2), \quad S_{21} \equiv -\frac{i}{\pi} \widehat{Q_{21}}(-2k_1, 2k_2).$$

Figure 3 demonstrates the effect of the truncation radius on the sharpness of the recovered admittivity for the best case scenario (idealized scattering data produced by solving (4) using (7) computed directly for

a known admittivity γ .) Note that as the radius increases, the image sharpens markedly. The conductivity images are analogous and thus omitted in the interest of space.

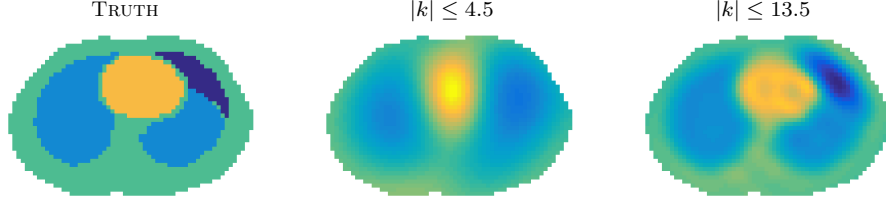


FIGURE 3. Recovery of permittivity from idealized scattering data, solution of the $\bar{\partial}_k$ equation (4) using the asymptotic condition $M \sim I$ for $|k| \leq 4.5$ and $|k| \leq 13.5$.

In addition to the low-pass filtering, another approximation is made when solving the D-bar equation (4). In practice, (4) is decoupled into two Lipmann-Schwinger type systems that are solved using the asymptotic behavior of the CGO solutions $M \sim I$:

$$(13) \quad \begin{cases} M_{11}(z, k) &= 1 + \frac{1}{\pi k} * [M_{12}(z, \bar{k})e(z, -k)S_{21}(k)] \\ M_{12}(z, k) &= 0 + \frac{1}{\pi k} * [M_{11}(z, \bar{k})e(z, \bar{k})S_{12}(k)] \end{cases}$$

$$\begin{cases} M_{21}(z, k) &= 0 + \frac{1}{\pi k} * [M_{22}(z, \bar{k})e(z, -k)S_{21}(k)] \\ M_{22}(z, k) &= 1 + \frac{1}{\pi k} * [M_{21}(z, \bar{k})e(z, \bar{k})S_{12}(k)], \end{cases}$$

where $*$ denotes convolution in k over the disc of radius R . Replacing the asymptotic conditions 1 and 0 with the corresponding finite integral approximations [Alsaker (2016); Alsaker and Mueller (2016); Hamilton et al. (2017)]

$$(14) \quad M_{ij}^{\text{int}}(z) = \frac{1}{\pi R^2} \int_{|k| \leq R} M_{ij}(z, k) dk, \quad i, j = 1, 2.$$

greatly improves the visual structure of the admittivity as well (see Figure 4). In practice this asymptotic replacement term cannot be computed as it requires knowledge of the true CGO solutions M for the true admittivity γ (generated by solving (2)). This is where *a priori* knowledge comes in very handy.

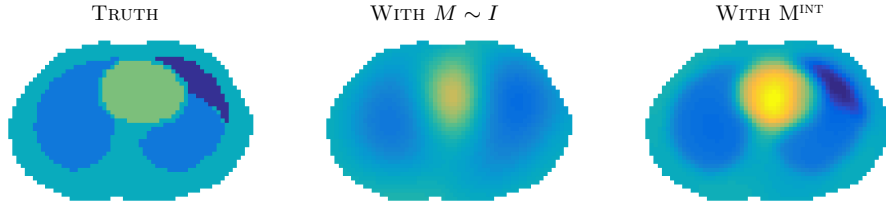


FIGURE 4. Recovery of permittivity from idealized scattering data, solution of the $\bar{\partial}_k$ equation (4) using vs the asymptotic replacement term, with a scattering radius of $|k| \leq 4.5$.

2.2. The A Priori D-bar Method for Admittivities. In most applications at least some knowledge of the approximate underlying structure is known, *a priori*. In particular, for thoracic EIT imaging a patient may have previous CT scan on file or can at least be matched to a representative CT image using an anatomical atlas. Such information can be used to build a spatial prior: approximate organ boundaries known with high-confidence, and values can be assigned from literature or by using average values from an initial admittivity reconstruction, etc.

Given such an admittivity prior γ_{PR} , the measurement scattering data $S(k)$ can be augmented to a larger disc of radius $R_2 \geq R$ using

$$(15) \quad S_{R, R_2}(k) := \begin{cases} S(k) & 0 < |k| \leq R \\ S^{\text{PR}} & R < |k| \leq R_2 \\ 0 & \text{else} \end{cases}$$

where $S^{\mathbf{PR}}$ denotes the scattering data corresponding to $\gamma_{\mathbf{PR}}$. Additionally, the asymptotic replacement term M^{int} in (14) can be computed using $\gamma_{\mathbf{PR}}$ by solving (2) for $M^{\mathbf{PR}}$ with $Q^{\mathbf{PR}}$ (via (3)). The effect of the prior can be controlled through the extended radius R_2 and the weighting of the asymptotic replacement term M^{int} via the parameter α in the modified version of the D-bar equations in (13)

$$(16) \quad \begin{cases} M_{11}(z, k) &= [\alpha + (1 - \alpha) M_{11}^{\text{int}}(z)] + \frac{1}{\pi k} * [M_{12}(z, \bar{k})e(z, -k)S_{21}(k)] \\ M_{12}(z, k) &= [0 + (1 - \alpha) M_{12}^{\text{int}}(z)] + \frac{1}{\pi k} * [M_{11}(z, \bar{k})e(z, \bar{k})S_{12}(k)] \\ M_{21}(z, k) &= [0 + (1 - \alpha) M_{21}^{\text{int}}(z)] + \frac{1}{\pi k} * [M_{22}(z, \bar{k})e(z, -k)S_{21}(k)] \\ M_{22}(z, k) &= [\alpha + (1 - \alpha) M_{22}^{\text{int}}(z)] + \frac{1}{\pi k} * [M_{21}(z, \bar{k})e(z, \bar{k})S_{12}(k)] \end{cases}$$

where $\alpha = 0$ corresponds to no doubt in the prior $\gamma_{\mathbf{PR}}$, and $\alpha = 1$ the greatest doubt. The solution method is summarized in the flowchart in Figure 5.

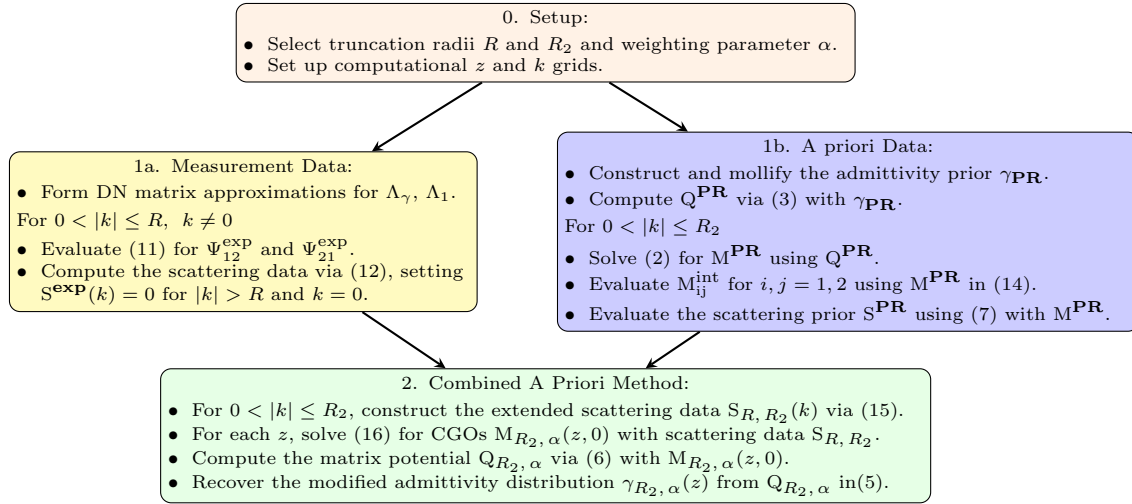


FIGURE 5. A Priori D-bar Method for Absolute Imaging

Notice that, for a given prior, Steps 1a and 1b of the flowchart are completely independent allowing for offline computation of Step 1b if desired. Furthermore, Steps 1a and 1b are trivially parallelizable in k and Step 2 is trivially parallelizable in z allowing for additional speedup.

2.3. Difference Imaging: The S^{diff} approximation. The D-bar methodology outlined above can also be applied to time-difference imaging. A *differencing-scattering transform* was first introduced in [Isaacson et al. (2006)] for real-valued conductivity-only imaging and in [Herrera et al. (2015)] for admittivities using the tangential derivative formulation. The concept can be extended to our complex-valued admittivity framework as follows.

The *differencing-scattering transform* S^{diff} is defined as the difference in approximate scattering data S^{exp} for admittivity γ and that for a reference measurement γ_{ref} :

$$S^{\text{diff}}(k) = S^{\text{exp}, \gamma}(k) - S^{\text{exp}, \gamma_{\text{ref}}}(k).$$

Hence, we have

$$(17) \quad \begin{aligned} S_{12}^{\text{diff}}(k) &= S_{12}^{\text{exp}, \gamma}(k) - S_{12}^{\text{exp}, \gamma_{\text{ref}}}(k) \\ &= \frac{i}{2\pi} \int_{\partial\Omega} e^{-i\bar{k}z} \Psi_{12}^{\text{exp}, \gamma}(z, k) \nu(z) dS(z) - \frac{i}{2\pi} \int_{\partial\Omega} e^{-i\bar{k}z} \Psi_{12}^{\text{exp}, \gamma_{\text{ref}}}(z, k) \nu(z) dS(z) \\ &= \frac{i}{2\pi} \int_{\partial\Omega} e^{-i\bar{k}z} \Psi_{12}^{\text{diff}}(z, k) \nu(z) dS(z), \end{aligned}$$

where

$$\begin{aligned}
 \Psi_{12}^{\text{diff}}(z, k) &= \Psi_{12}^{\text{exp}, \gamma}(k) - \Psi_{12}^{\text{exp}, \gamma_{\text{ref}}}(k) \\
 &= \frac{i}{4\pi k} \int_{\partial\Omega} \frac{e^{i\bar{k}(z-\zeta)}}{z-\zeta} (\Lambda_{\gamma} - \Lambda_1) e^{-ik\bar{\zeta}} ds(\zeta) - \frac{i}{4\pi k} \int_{\partial\Omega} \frac{e^{i\bar{k}(z-\zeta)}}{z-\zeta} (\Lambda_{\gamma_{\text{ref}}} - \Lambda_1) e^{-ik\bar{\zeta}} ds(\zeta) \\
 (18) \quad &= \int_{\partial\Omega} \frac{e^{i\bar{k}(z-\zeta)}}{z-\zeta} (\Lambda_{\gamma} - \Lambda_{\gamma_{\text{ref}}}) \frac{e^{-ik\bar{\zeta}}}{-ik} ds(\zeta).
 \end{aligned}$$

In an analogous fashion,

$$(19) \quad S_{21}^{\text{diff}}(k) = -\frac{i}{2\pi} \int_{\partial\Omega} e^{i\bar{k}z} \Psi_{21}^{\text{diff}}(z, k) \overline{\nu(z)} dS(z),$$

$$(20) \quad \Psi_{21}^{\text{diff}}(z, k) = \int_{\partial\Omega} \left[\frac{e^{ik(z-\zeta)}}{z-\zeta} \right] (\Lambda_{\gamma} - \Lambda_{\gamma_{\text{ref}}}) \frac{e^{ik\zeta}}{ik} ds(\zeta).$$

A difference imaging approach with the *differencing scattering transform* S^{diff} can then be developed by replacing Step 1 in Section 2 with Equations (17) through (20), then computing Steps 2 and 3 with $S^{\text{diff}}(k)$ in place of the scattering data S^{exp} . The reconstructed time-difference image for γ^{diff} is then formed by subtracting 1 (the background admittivity). If the background admittivity is not 1, a scaling can be used as in the case of absolute EIT imaging (Section 2.1). The scaling is slightly different for difference imaging. As before, Λ_{γ} and $\Lambda_{\gamma_{\text{ref}}}$ are scaled by the best constant admittivity fit γ_{best} , and the resulting admittivity re-scaled by γ_{best} . Then, to produce γ^{diff} , the background admittivity γ_{best} is subtracted. The schematic in Figure 6 describes the time-differencing D-bar Method for complex admittivities.

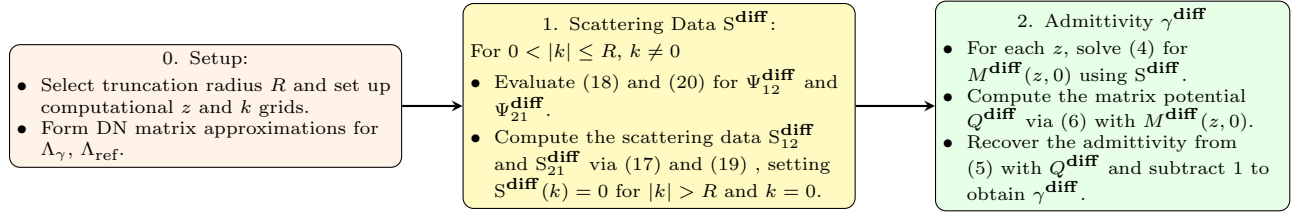


FIGURE 6. D-bar Method for Time-Difference Imaging

2.4. Difference Imaging with a A Priori information. *A priori* information can also be included into time-difference imaging. One option is to include the same spatial prior (approximate organ/structure locations) as was used in the absolute EIT imaging setting, but instead assign the admittivity values of the prior from an initial time-difference image (e.g. using the method described in Section 2.3, or from any other time-differencing method). Alternatively, one could build a spatial prior by extracting boundaries from an initial time-difference image using segmentation. Once a prior is obtained, a similar *a priori* D-bar method can be employed for time-differencing EIT, as described by the flowchart in Figure 7.

3. RESULTS

3.1. Experimental Setup. In this work we apply the solution methods to experimental data taken using two different EIT machines: ACT3 and ACT4 from Rensselaer Polytechnic Institute.

The archival ACT3 data used agar targets of a heart (0.75 S/m) a two lungs (0.24 S/m) in a saline bath of 0.424 S/m filled to a height of 1.6cm. The targets were placed in a circular tank of radius 15cm with 32 electrodes of width 2.5cm and trigonometric current patterns were used with an amplitude of 0.2mA and frequency 28.8kHz (see Isaacson et al. (2004) for additional experimental details).

The archival ACT4 data used agar heart a lung targets as well. The conductivity of the heart was approximately 0.5 S/m and the lungs 0.1 S/m. Graphite was added to the agar to create a susceptibility of approximately 0.03 S/m at the applied 33kHz [Muller (2014); Muller et al. (2013)]. Trigonometric voltage patterns of maximum amplitude 0.5V were applied (ACT4 applies voltages and measures currents) on an

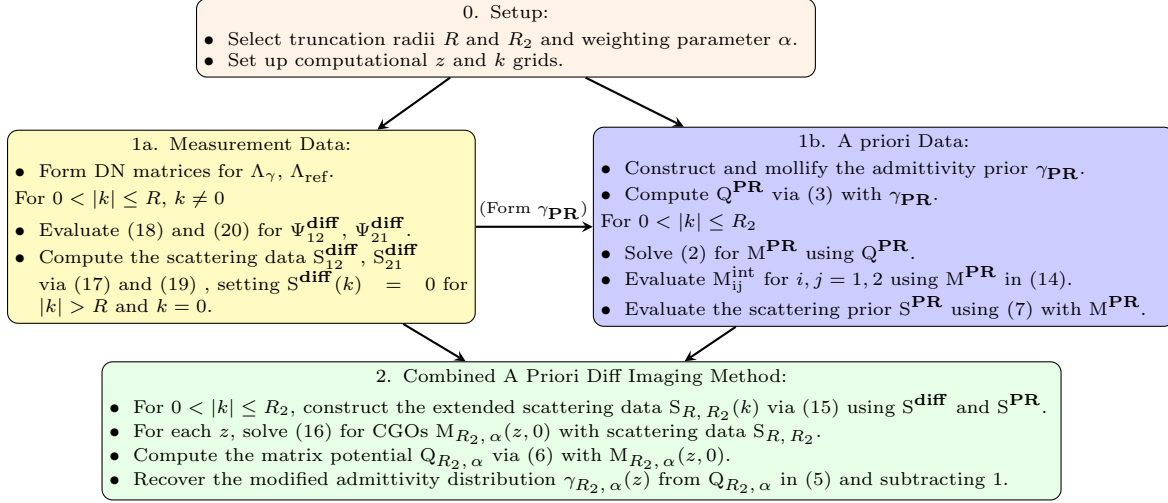


FIGURE 7. A Priori D-bar Method for Time-Difference Imaging



FIGURE 8. Experimental Setups for two different EIT machines: ACT3 and ACT4 from RPI. Agar targets simulating a chest phantom with a heart and lungs are used.

elliptical tank with principal semi-axes of length 16.5cm and 11.9cm and 32 electrodes each of width 2.5cm. The agar targets were in a saline bath of 0.224 S/m filled to a height of 2.51cm. To reconstruct the admittivity, the measured currents and voltages of the ACT4 data were used to synthesize the voltages that would have occurred if 1mA maximum amplitude trigonometric currents patterns were applied.

3.2. Implementing the Algorithms. The discrete matrix approximations R_γ (to the ND map \mathcal{R}_γ) and L_γ (to the DN map Λ_γ) were formed using discrete inner products as described in Isaacson et al. (2004). Recall that the absolute images require a simulated DN map Λ_1 (see (9) and (10)). The boundaries for the respective domains were formed by clicking around the edge of the tanks in the photos shown in Figure 8 and a parameterized boundary function was created using Fourier Series as in [Jain (1997)]. The DN map Λ_1 was then simulated using FEM. It should be noted that the FEM solver was not finely tuned to the intricacies of the different systems.

The priors were formed using the photos in Figure 8. See Figure 9 for the boundaries of the respective priors. For the the ACT4 Heart and one lung data, two priors were tested: a heart and two lungs (Prior 1) as well as a heart and only one lung (Prior 2).

The interested reader is referred to [Hamilton et al. (2012)] for a detailed numerical implementation of the D-bar method for absolute imaging (Figure 2), and [Hamilton et al. (2017)] for the numerical implementation of the *a priori* method. The numerical solution technique for the time-differencing D-bar methods are analogous and thus omitted in the interest of space. The admittivities were reconstructed on a 64×64 spatial z -grid using the measurement scattering data S^{exp} computed on a 32×32 k -grid. As the scattering data is unstable for high frequencies (as it blows up in magnitude), the data is only computed for $|k| \leq R$, for a given radius R . Additionally, the scattering data may blow up in some directions faster than others and therefore a thresholding condition is added. A common threshold of 0.3 was used across all examples

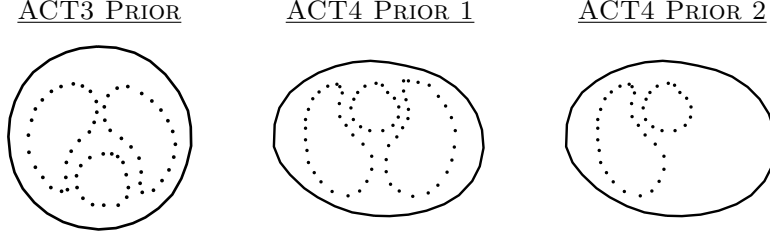


FIGURE 9. From left to right. The boundaries of the ACT3 agar data and the boundaries for the ACT4 agar data. Reconstructions of the heart with one lung are performed using ‘ACT4 Prior 1’ and compared to those from ‘ACT4 Prior 2’.

(i.e., any scattering data $S_{12}^{\text{exp}}(k)$ or $S_{21}^{\text{exp}}(k)$ for which the magnitude of the real or imaginary parts exceeded 0.3 was set to zero). The choice of scattering radius R was also fixed across all examples at $R = 4.0$. For clinical implementation, training data sets could be used to determine appropriate common thresholds and radii but this is outside the scope of this work.

3.3. Experimental Results: ACT3 Agar targets. We begin with the ACT3 data with agar targets. The absolute and time-difference D-bar reconstructions for the heart with two lungs are shown in the top and bottom rows of Figure 10 with the approximate target locations are outlined in black dots. The priors γ_{PR} were formed using the average pixel value in each region (Absolute: heart=0.6418, left lung=0.2932, right lung=0.2998, Time Difference: heart=0.1751, left lung=-0.1323, right lung=-0.1255) extracted from the corresponding reconstructed D-bar images. The scattering prior S^{PR} was then formed using γ_{PR} and combined with the original scattering data (S^{exp} and S^{diff} respectively). Then the new conductivity was reconstructed via the corresponding *a priori* method (absolute or time-difference) using the increased radius $R_2 = 5.33$ and $\alpha = 1, \frac{2}{3}$, and 0.

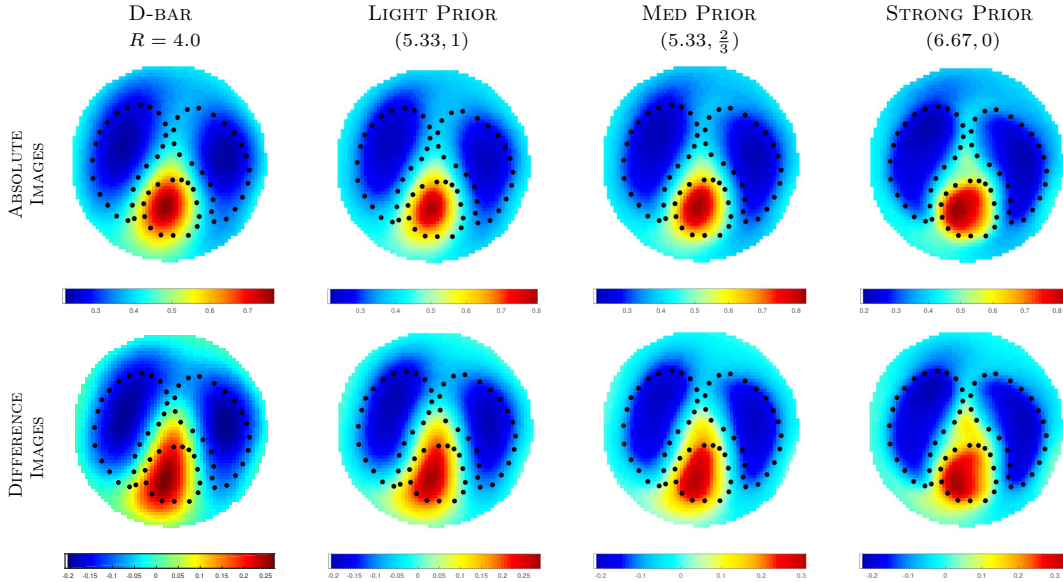


FIGURE 10. Comparison of conductivity reconstructions for ACT3 data on an agar chest phantom. Top: Absolute conductivity reconstructions. Bottom: Time-difference conductivity reconstructions. D-bar results are compared to those using the ‘ACT3 prior’ and average extracted regional values for various parameter pairs (R_2, α) .

In the absolute D-bar conductivity reconstruction, the maximum value in the heart region was 0.769 S/m and the minimum in the lungs was 0.221 S/m. Table 1 tracks the average regional admittivity values for the absolute images displayed in Figure 10 as spatial *a priori* information is included.

TABLE 1. Reconstructed admittivity average values (S/m) for the ACT3 Heart & Lungs data.

	D-BAR	LIGHT PRIOR	MED PRIOR	STRONG PRIOR
HEART	0.6418	0.6499	0.6787	0.7068
L. LUNG	0.2932	0.2856	0.2785	0.2694
R. LUNG	0.2998	0.2899	0.2814	0.2701

3.4. Experimental Results: ACT4 Agar targets. Next we explore the ACT4 data for the elliptical tank. The absolute and time-difference D-bar reconstructions for the heart with two lungs are shown in the top and bottom rows of Figure 11, respectively, where approximate target locations are outlined with black dots. The average pixel value in each region (Absolute: heart= $0.6219 + 0.1323i$, left lung= $0.1769 + 0.0258i$, right lung= $0.2053 + 0.0328i$, Time Difference: heart= $0.2687 + 0.1025i$, left lung= $-0.0867 + 0.0229i$, right lung= $-0.0652 + 0.0267i$) were extracted from the reconstructed D-bar images and used to form the admittivity prior γ_{PR} . The new admittivity was reconstructed via the corresponding *a priori* method (absolute or time-difference) using the increased radius $R_2 = 5.33$ and $\alpha = \frac{2}{3}, \frac{1}{3}$. Recall that $\alpha = 1$ represents full doubt in the prior and thus the choice of $\alpha = \frac{2}{3}$ with a slight increase in R_2 is a mild inclusion of the prior yet still results in significant improvement in localization of the heart and lungs for both the absolute and time-difference imaging cases.

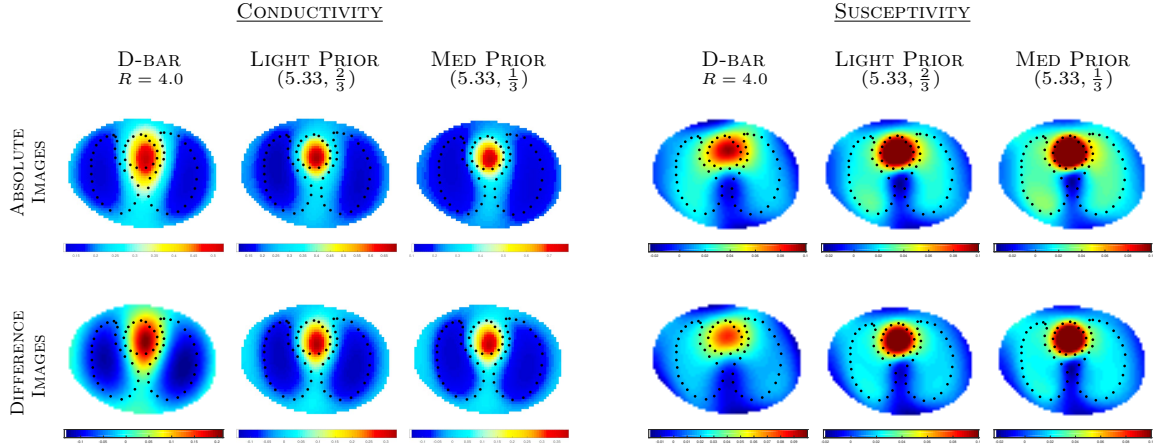


FIGURE 11. Absolute and time-difference D-bar admittivity reconstructions of the ACT4 chest phantom with two lungs. Results are compared to those using the ‘ACT4 Prior 1’ with average extracted values using parameter pairs (R_2, α) . The colormap on the susceptibility images is maxed out at 0.1 S/m.

In the absolute D-bar admittivity reconstruction, the maximum value in the heart region was $0.527 + 0.097i$ S/m and the minimum in the lungs was $0.125 - 0.013i$ S/m. Table 2 tracks the average regional admittivity values for the absolute images displayed in Figure 11 as spatial *a priori* information is included.

TABLE 2. Reconstructed admittivity average values (S/m) for the ACT4 Heart & Lungs data.

	D-BAR	LIGHT PRIOR	MED PRIOR
HEART	$0.4298 + 0.0737i$	$0.5270 + 0.1205i$	$0.5806 + 0.1427i$
L. LUNG	$0.1763 + 0.0227i$	$0.1622 + 0.0250i$	$0.1579 + 0.0246i$
R. LUNG	$0.1979 + 0.0194i$	$0.1859 + 0.0229i$	$0.1821 + 0.0242i$

Next, Figures 12 and 13 present the absolute and time-difference D-bar reconstructions for the heart with one lung. The absolute images were formed using the S^{exp} approximation. The approximate target locations are outlined with black dots. Priors 1 and 2 were tested even though the phantom contains only one lung: Figure 12 uses Prior 1 (two lungs), whereas Figure 13 uses Prior 2 (one lung). Average pixel values from each region (Absolute: heart= $0.3979 + 0.0899i$, left lung= $0.1710 + 0.0264i$, right lung= $0.3208 + 0.0017i$, Time Difference: heart= $0.1115 + 0.0767i$, left lung= $-0.0773 + 0.0231i$, right lung= $0.0296 + 0.0046i$) were extracted

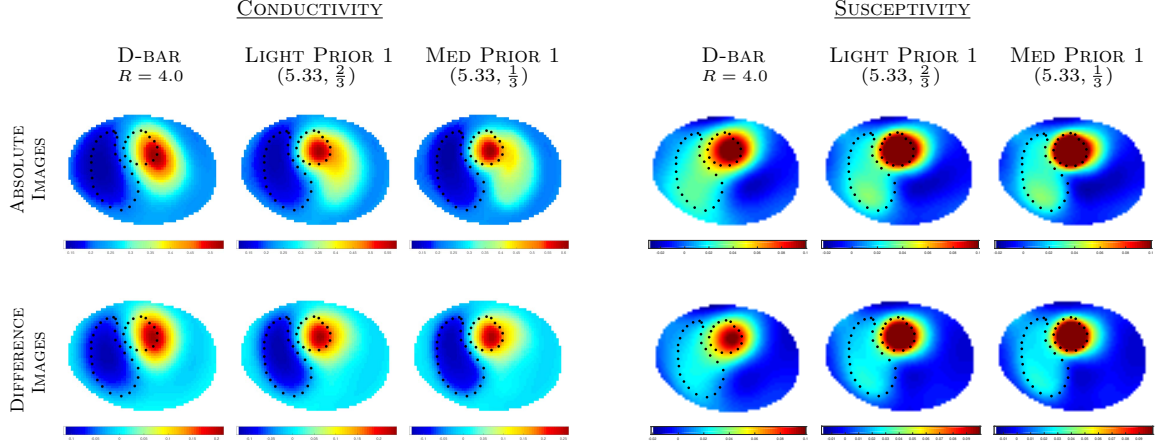


FIGURE 12. Absolute and time-difference D-bar admittivity reconstructions of the ACT4 chest phantom with one lung data. Results are compared to those using the ‘ACT4 Prior 1’ with average extracted values using parameter pairs (R_2, α) . The colormap on the susceptibility images is maxed out at 0.1 S/m.

from the reconstructed D-bar images and used to form the admittivity prior γ_{PR} . The results are compared to those resulting from including *a priori* data using parameters $R_2 = 5.33$ and $\alpha = \frac{2}{3}, \frac{1}{3}$. Figure 13 presents the analogous results to Figure 12 but instead using the ‘ACT4 Prior 2’ which only contains the heart and left lung.

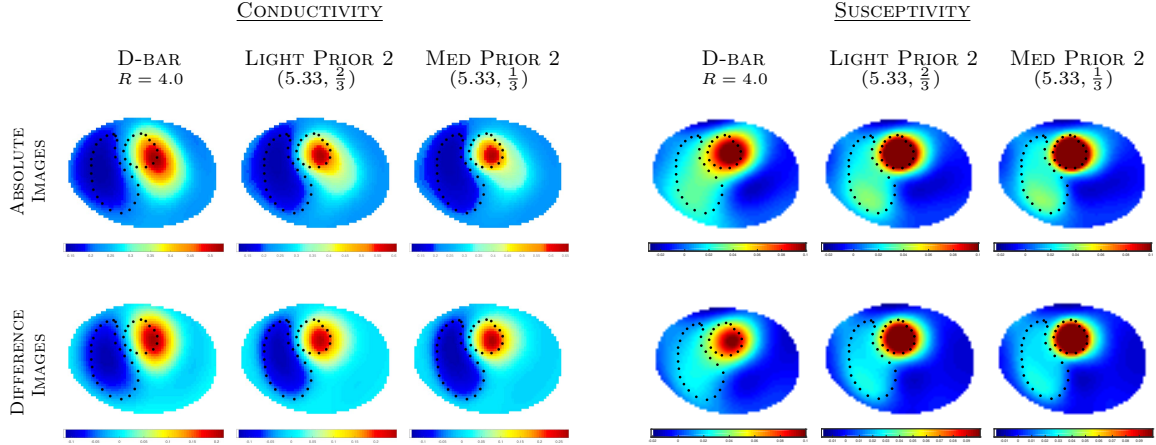


FIGURE 13. Absolute and time-difference D-bar admittivity reconstructions of the ACT4 chest phantom with one lung data. Results are compared to those using the ‘ACT4 Prior 2’ with average extracted values using parameter pairs (R_2, α) . The colormap on the susceptibility images is maxed out at 0.1 S/m.

In the absolute D-bar admittivity reconstruction of the heart and one lung, the maximum value in the heart region was $0.5335 + 0.1234i$ S/m and the minimum in the lung was $0.1374 + 0.0085i$ S/m. Table 3 tracks the average regional admittivity values for the absolute images displayed in Figures 12 and 13 as spatial *a priori* information is included for the two priors: two vs. one lung(s).

4. DISCUSSION

Figures 10, 11, 12, and 13 demonstrate that the D-bar method (flowchart in Fig 2) can produce high-quality absolute (static) EIT images. We remind the reader that the DN map Λ_1 was simulated with imprecise knowledge of the boundary and electrode locations (estimated from the photographs in Figure 8)

TABLE 3. Reconstructed admittivity average values (S/m) for the ACT3 Heart & Lung data using Priors 1 and 2.

	D-BAR	LIGHT PRIOR 1	MED PRIOR 1	LIGHT PRIOR 2	MED PRIOR 2
HEART	$0.3979 + 0.0899i$	$0.4616 + 0.1427i$	$0.4911 + 0.1665i$	$0.4697 + 0.1441i$	$0.5043 + 0.1685i$
L. LUNG	$0.1710 + 0.0264i$	$0.1592 + 0.0287i$	$0.1549 + 0.0289i$	$0.1583 + 0.0287i$	$0.1537 + 0.0288i$

and was not tuned to the particular EIT device (ACT3 or ACT4). Such a fine-tuning of the forward model used for Λ_1 would likely result in further improved absolute images. Note that using the two lungs prior for the ACT4 ‘Heart & Lung’ data has a minimal effect on reconstructions compared to using the prior with only one lung (compare Figures 12 and 13), with the change only being notable for the decrease in the artifact to the right of the lung in the absolute conductivity images. Additionally, the time-difference images demonstrate that the new *a priori* time-difference method (flowchart in Fig 7) can be useful as well to sharpen classical time-difference images.

The absolute D-bar method was able to recover the admittivity values of the phantoms for the all but the ACT4 susceptibility of the heart. In particular, the conductivity of the ACT3 phantom was recovered to within 2.5% for the heart, and 7.9% for the lungs. The average regional values improved with the introduction of the prior data even though only average regional values from the initial D-bar image were used.

Including *a priori* information (spatial prior with admittivity values assigned either from literature or extracted average values from an initial EIT reconstruction) significantly sharpens the boundaries of inclusions. In all cases, it is clear that the spatial resolution of the boundaries of the inclusions improves as the prior is weighted more heavily (as $\alpha \rightarrow 0$ and R_2 increases) even though only regional average values are used for the prior. It is also clear that the S^{exp} reconstruction (absolute EIT) was stable enough for the experimental setting, and as it bypasses the need to compute the CGO solutions u_1 and u_2 in (10), the method is faster than the full nonlinear D-bar method.

5. CONCLUSION

This preliminary work demonstrates three main things: 1) quality information can be gathered from absolute EIT images using the D-bar method [Hamilton et al. (2012)] on experimental tank data, 2) the *a priori* admittivity D-bar method is stable enough for experimental tank data, 3) *a priori* information can also be included into time-differencing EIT resulting in sharpened images of experimental data.

Moreover, the first absolute EIT reconstructions of a complex admittivity from a D-bar method are presented. The forward model used to generate Λ_1 was not fine-tuned to the specific EIT machines used therefore demonstrating promising robustness of the method. Absolute EIT reconstructions will likely improve if the forward model used for Λ_1 is specific to the EIT device.

By forming the prior from pictures (and clicks in MATLAB) as well as assigning values from the average of the regional reconstructed EIT values, bias in the prior was limited. Using more accurate knowledge of the prior (e.g. from a CT/MRI/ultrasound scan and more precise admittivity values), would improve results. A more detailed study of the effect of the quality of the prior on the reconstructions is the subject of future work, outside the scope of this proof of concept presentation.

ACKNOWLEDGEMENTS

The tank data were supplied by the EIT group at RPI [<https://www.ecse.rpi.edu/homepages/saulnier/eit/eit.html>] and Peter Muller (now at Colorado State University), for which we express our thanks. The author also thanks the EIT labs at RPI, CSU, and University of São Paulo for their insights into working with experimental data.

REFERENCES

- Melody Alsaker. *Computational Advancements in the D-bar Reconstruction Method for 2-D Electrical Impedance Tomography*. PhD thesis, Colorado State University, 2016.
- Melody Alsaker and Jennifer L. Mueller. A D-bar algorithm with *a priori* information for 2-D Electrical Impedance Tomography. *SIAM J. on Imaging Sciences*, 9(4):1619–1654, 2016.
- K. Astala and L. Päiväranta. A boundary integral equation for Calderón’s inverse conductivity problem. In *Proc. 7th Internat. Conference on Harmonic Analysis, Collectanea Mathematica*, 2006a.

- K. Astala and L. Päiväranta. Calderón's inverse conductivity problem in the plane. *Annals of Mathematics*, 163(1): 265–299, 2006b. ISSN 0003-486X. doi: 10.4007/annals.2006.163.265. URL <http://dx.doi.org/10.4007/annals.2006.163.265>.
- N.J. Avis and D.C. Barber. Incorporating a priori information into the Sheffield filtered backprojection algorithm. *Physiological Measurement*, 16(3A):A111–A122, 1995.
- U. Baysal and B.M. Eyüboğlu. Use of a priori information in estimating tissue resistivities - a simulation study. *Physics in Medicine and Biology*, 43(12):3589–3606, 1998.
- R. M. Brown and G. Uhlmann. Uniqueness in the inverse conductivity problem for nonsmooth conductivities in two dimensions. *Communications in Partial Differential Equations*, 22(5):1009–1027, 1997.
- M. Brühl. Explicit characterization of inclusions in electrical impedance tomography. *SIAM Journal on Mathematical Analysis*, 32:1327–1341, 2001.
- M. Brühl and M. Hanke. Numerical implementation of two non-iterative methods for locating inclusions by impedance tomography. *Inverse Problems*, 16:1029–1042, 2000.
- M. Brühl, M. Hanke, and M.S. Vogelius. A direct impedance tomography algorithm for locating small inhomogeneities. *Numerische Mathematik*, 93(4):635–654, 2003.
- A.-P. Calderón. On an inverse boundary value problem. In *Seminar on Numerical Analysis and its Applications to Continuum Physics (Rio de Janeiro, 1980)*, pages 65–73. Soc. Brasil. Mat., Rio de Janeiro, 1980.
- Daniela Calvetti, Paul J Hadwin, Janne MJ Huttunen, David Isaacson, Jari P Kaipio, Debra McGivney, Erkki Somersalo, and Joseph Volzer. Artificial boundary conditions and domain truncation in electrical impedance tomography. part i: Theory and preliminary results. *Inverse Problems & Imaging*, 9(3):749–766, 2015a.
- Daniela Calvetti, Paul J Hadwin, Janne MJ Huttunen, Jari P Kaipio, and Erkki Somersalo. Artificial boundary conditions and domain truncation in electrical impedance tomography. part ii: Stochastic extension of the boundary map. *Inverse Problems & Imaging*, 9(3):767–789, 2015b.
- M. Cheney, D. Isaacson, and E.L. Isaacson. Exact solutions to a linearized inverse boundary value problem. *Inverse Problems*, 6:923–934, 1990.
- H. Dehghani, D.C. Barber, and I. Basarab-Horwath. Incorporating a priori anatomical information into image reconstruction in electrical impedance tomography. *Physiological Measurement*, 20(1):87–102, 1999.
- D. C. Dobson and F. Santosa. An image enhancement technique for electrical impedance tomography. *Inverse Problems*, 10:317–334, 1994.
- Melody Dodd and Jennifer L. Mueller. A real-time d-bar algorithm for 2-d electrical impedance tomography data. *Inverse Problems and Imaging*, 8(4):1013–1031, 2014. ISSN 1930-8337. doi: 10.3934/ipi.2014.8.1013. URL <http://aimsciences.org/journals/displayArticlesnew.jsp?paperID=10528>.
- P.M. Edic, D. Isaacson, G.J. Saulnier, H. Jain, and J.C. Newell. An iterative newton-raphson method to solve the inverse admittivity problem. *IEEE Transactions on Biomedical Engineering*, 45(7):899–908, Jul. 1998.
- L. D. Faddeev. Increasing solutions of the Schrödinger equation. *Soviet Physics Doklady*, 10:1033–1035, 1966.
- D. Ferrario, B. Grychtol, A. Adler, J. Sola, S.H. Böhm, and M. Bodenstein. Toward morphological thoracic EIT: Major signal sources correspond to respective organ locations in CT. *Biomedical Engineering, IEEE Transactions on*, 59(11):3000–3008, 2012.
- E. Francini. Recovering a complex coefficient in a planar domain from Dirichlet-to-Neumann map. *Inverse Problems*, 16:107–119, 2000.
- B. Gebauer and N. Hyvönen. Factorization method and irregular inclusions in electrical impedance tomography. *Inverse Problems*, 23:2159–2170, 2007.
- S. J. Hamilton, J. L. Mueller, and M. Alsaker. Incorporating a spatial prior into nonlinear D-Bar EIT imaging for complex admittivities. *IEEE Trans. Med. Imaging*, 36(2):457–466, 2017.
- Sarah J Hamilton and Jennifer L Mueller. Direct eit reconstructions of complex admittivities on a chest-shaped domain in 2-d. *IEEE transactions on medical imaging*, 32(4):757–769, 2013.
- S.J. Hamilton, C.N.L. Herrera, J. L. Mueller, and A. VonHerrmann. A direct D-bar reconstruction algorithm for recovering a complex conductivity in 2-D. *Inverse Problems*, 28:(095005), 2012.
- Bastian Harrach and Jin Keun Seo. Detecting inclusions in electrical impedance tomography without reference measurements. *SIAM J. Appl. Math.*, 69(6):1662–1681, 2009. ISSN 0036-1399. doi: 10.1137/08072142X. URL <http://dx.doi.org/10.1137/08072142X>.
- C. N. L. Herrera. *Um método D-bar para estimar admitividade em 2-D através de tomografia por impedância elétrica*. Ph.D. Thesis, University of São Paulo, São Paulo, Brazil, Fall 2012.
- C.N.L. Herrera, M.F.M. Vallejo, J.L. Mueller, and R.G. Lima. Direct 2-d reconstructions of conductivity and permittivity from eit data on a human chest. *Medical Imaging, IEEE Transactions on*, 34(1):267–274, Jan 2015. ISSN 0278-0062. doi: 10.1109/TMI.2014.2354333.
- N. Hyvönen. Application of the factorization method to the characterization of weak inclusions in electrical impedance tomography. *Advances in Applied Mathematics*, 39:197–221, 2007.

- D. Isaacson, J. L. Mueller, J. C. Newell, and S. Siltanen. Reconstructions of chest phantoms by the D-bar method for electrical impedance tomography. *IEEE Transactions on Medical Imaging*, 23:821–828, 2004.
- D. Isaacson, J.L. Mueller, J.C. Newell, and S. Siltanen. Imaging cardiac activity by the D-bar method for electrical impedance tomography. *Physiological Measurement*, 27:S43–S50, 2006.
- H. Jain. *Electrical impedance tomography of conductivity and permittivity distributions in arbitrary geometries using regularized algorithms*. PhD thesis, Rensselaer Polytechnic Institute, 1997.
- H. Jain, D. Isaacson, P.M. Edic, and J.C. Newell. Electrical impedance tomography of complex conductivity distributions with noncircular boundary. *IEEE Transactions on Biomedical Engineering*, 44(11):1051–1060, Nov. 1997.
- JP Kaipio, V. Kolehmainen, M. Vauhkonen, and E. Somersalo. Inverse problems with structural prior information. *Inverse problems*, 15:713–729, 1999.
- J.P. Kaipio, V. Kolehmainen, E. Somersal, and M. Vauhkonen. Statistical inversion and monte carlo sampling methods in electrical impedance tomography. *Inverse Problems*, 16(5):1487–1522, 2000.
- K. Knudsen, M. Lassas, J.L. Mueller, and S. Siltanen. Regularized D-bar method for the inverse conductivity problem. *Inverse Problems and Imaging*, 3(4):599–624, 2009.
- J.L. Mueller and S. Siltanen. *Linear and Nonlinear Inverse Problems with Practical Applications*. SIAM, 2012.
- P. Muller. *Numerical Methods of Electrical Impedance Tomography*. PhD thesis, Rensselaer Polytechnic Institute, 2014.
- P. A. Muller, D. Isaacson, J. C. Newell, and G. J. Saulnier. Calderón’s method on an elliptical domain. *Physiological Measurement*, 32:609–622, 2013.
- A. I. Nachman. Global uniqueness for a two-dimensional inverse boundary value problem. *Annals of Mathematics*, 143:71–96, 1996.
- R.G. Novikov. A multidimensional inverse spectral problem for the equation $-\delta\psi + (v(x) - eu(x))\psi = 0$. *Functional Analysis and Its Applications*, 22(4):263–272, 1988.
- M. Soleimani. Electrical impedance tomography imaging using a priori ultrasound data. *BioMedical Engineering OnLine*, 5(8), 2006.
- M. Vauhkonen, D. Vadász, P. A. Karjalainen, E. Somersalo, and J. P. Kaipio. Tikhonov regularization and prior information in electrical impedance tomography. *IEEE Transactions on Medical Imaging*, 17:285–293, 1998.